Towards Durable Practical Lithium-Metal Batteries: Advancing the Feasibility of Poly-DOL-Based Quasi-Solid-State Electrolytes via a Novel Nitrate-Based Additive

Zilong Wang,[a] Yuhao Wang,[a] Longyun Shen,[a] Zhaoqing Jin,[b] Ho Mei Law,[c] Anbang Wang,[b] Weikun Wang,[b],* Francesco Ciucci[a,c,d],*

a. Department of Mechanical and Aerospace Engineering, The Hong Kong University of Science and Technology, Clear Water Bay, Kowloon, Hong Kong SAR, China

b. Beijing Key Laboratory of Advanced Chemical Energy Storage Technology and Materials, Research Institute of Chemical Defense, Beijing, 100191, China

c. Chair of Electrode Design for Electrochemical Energy Systems, University of Bayreuth, Bayreuth, Germany

d. Bavarian Center for Battery Technology (BayBatt), 95448 Bayreuth, Bavaria, German E-mail: francesco.ciucci@uni-bayreuth.de

* Corresponding author. E-mail: <u>francesco.ciucci@uni-bayreuth.de</u> (Francesco Ciucci).

* Corresponding author. E-mail: <u>wangweikun2002@163.com</u> (Weikun Wang).

Calculations

Molecular dynamics (MD) calculations: MD simulations were carried out with GROMACS[1] 2021.6. The OPLS-AA force field[2] and restrained electrostatic potential (RESP) charge (obtained with Multiwfn[3, 4]) were used. Bonds with hydrogen atoms were constrained using the linear constraint solver (LINCS) algorithm[5]. The initial atomic coordinates were generated with Packing Optimization for Molecular Dynamics Simulations (Packmol) program[6]. Initially, the box was set to be $80 \times 80 \times 80 \text{Å}^3$, with periodic boundary conditions applied in all three directions. Then, 60 poly-DOL (degree of polymerization set at 10), 450 DME, 100 LiTFSI, and 60 TEGDN (or without TEGDN) molecules were added to the box. First, the model system was relaxed for 5.0 ns (time step = 1 fs) under a canonical ensemble (NVT). Then, it was equilibrated for 5.0 ns (time step = 1 fs) under an isothermal-isobaric (NPT) ensemble. After that, a simulation lasting 20 ns (time step = 1 fs) was carried out. The temperature for NPT equilibration and NVT trajectory production was controlled at 298 K using Nosé-Hoover temperature coupling. The pressure for NPT equilibration was held at 1 bar using Parrinello-Rahman pressure coupling. Particle-Mesh-Ewald (PME) method[7, 8] (cut-off distance = 1.0 nm) was used to treat the electrostatic interactions. The simulation results were visualized using Vesta[9]. The RDF, $g(r)$, of a certain species was calculated using the following expression:

$$g(r) = \frac{n_r}{4\pi r^2 \rho \Delta r} \tag{1}$$

where r is the distance of a shell atom from the reference atom, ρ is the average probability density of a species in the electrolyte, and n_r is the average number of atoms

within a shell of thickness Δr over the entire simulation time. By integrating $g(r)$ with respect to r, the CN of each specie surrounding the Li^+ center was obtained.

Density functional theory (DFT) calculations: DFT calculations were executed via Gaussian 09[10] software. The geometry optimizations incorporated Becke's three-parameter (B3) exchange functional in conjunction with the Lee-Yang-Parr (LYP) nonlocal correlation functional (termed B3LYP)[11], utilizing a 6-311G(d,p) basis set. Energy computations were performed using the CCSD/cc-pVTZ basis set to enhance calculation accuracy. The electrostatic potential analysis, along with the investigation of bond and dihedral angles, was done using GaussView 5.0.9[12] software. Visualization and rendering of the Highest Occupied Molecular Orbital (HOMO) and Lowest Unoccupied Molecular Orbital (LUMO) were conducted with the aid of the tools Multiwfn[3, 4] and VMD[13].

Experiments

Materials: Triethylene glycol (69%, Aladdin), concentrated nitric acid (69%, VWR), and concentrated sulfuric acid (95%, Ther. Sci. Chem) were used without further treatment. The solvents, 1,2-dimethoxyethane (DME) and 1,3-dioxolane (DOL), were purchased from Guangdong Canrd New Energy Technology Co. Ltd. and dried using 4 Å molecular sieves. The lithium salts, lithium bis(trifluoromethanesulfonyl)imide (LiTFSI, 99.95%), lithium hexafluorophosphate (LiPF$_6$, 99%), and lithium nitrate (LiNO$_3$, 99.99%) were purchased from Sigma-Aldrich and used without further treatment.

Preparation of TEGDN: TEGDN was synthesized via the nitrification of triethylene glycol using an ice bath. The process was initiated by adding 20 mL of concentrated sulfuric acid to a three-necked flask. This step was followed by the gradual addition of 50 mL of concentrated nitric acid to the same flask. Subsequently, 8 mL of triethylene glycol was introduced into the mixture. The resulting solution was then carefully transferred into iced deionized (DI) water, and the mixture was continually washed with additional DI water until a pH of 7.0 was achieved. The resulting product was collected using a separating funnel and was preserved with a 4 Å molecular sieve for future use.

Preparation of QSSE: The proportions of DOL, DME, and TEGDN were systematically varied, while the concentrations of LiPF$_6$ and LiTFSI were kept constant. Taking the preparation of a QSSE (*i.e.*, 1.0 M LiTFSI with 50 wt% of DOL, 45 wt% of DME and 5 wt% TEGDN, DOL wt% = wDOL/(wDOL + wDME + wTEGDN)) as an example, first, 250 mg of DOL, 225 mg of DME, 25 mg of TEGDN

and 144 mg of LiTFSI were mixed into a sealed vial. Second, 38 mg of $LiPF_6$ were added into the sealed vial. After 20 mins employed for the dissolution of $LiPF_6$, the solution was injected into the prepared coin-type or pouch-type cell. Next, the cell was assembled and sealed. The precursor solution subsequently underwent spontaneous *in situ* polymerization in the cell at room temperature to form the QSSE. The polymerization process took 7 hours (Figure S7). All electrolyte preparation and coin-type cell fabrication processes were performed inside a glove box (Mikrouna, $[O_2]$ < 0.1 ppm, $[H_2O]$ < 0.1 ppm) filled with ultrapure Ar (≥99.999%, Air Products).

Preparation for Li-S batteries: The sulfur-composite material (SCM) was prepared as described in the literature[14]. The SCM contains 82 wt % of S. Conductive carbon, catalysts, and binder take up the rest of the weight.

For the pouch-type Li-S cells, the SCM was directly used as cathode materials. Each pouch-type cell contained four 50 mm × 75 mm cathode foils, with the mass loading of each electrode being ~9.06 mg cm^{-2} (~4.53 mg cm^{-2} for single side). The size of lithium anode foil in each pouch-type cell was around 270 mm × 90 mm and the thickness of lithium anode foil was around 150 μm. The calculated N/P ratio was around 2.68.

For the coin-type Li-S cells, the SCM (80 wt %), CNT (7 wt %), acetylene black (7 wt %, as conductive agent), and LA133 (6 wt %, as binder) were prepared in advance and added into an aqueous solution of isopropanol and stirred for 10 h. The obtained cathode slurries were coated on aluminum foil using an automatic coating machine and dried in

a vacuum oven at 55 °C for 24 h. The diameter of the electrode disks for the coin-type cell was 12 mm, and the sulfur mass loading in each electrode disk was 1.25 mg cm^{-2}.

Preparation of LFP & NCM811 cathode for coin-type batteries: The LFP (Guangdong Canrd New Energy Technology Co. Ltd.) slurry was prepared by mixing LFP powder, conductive carbon black (TIMCAL Super P, MTI), and polyvinylidene difluoride (PVDF) binder at a weight ratio of 8:1:1 in N-methyl-2-pyrrolidone (NMP, 99.9%, MTI) solvent. The slurry was then magnetically stirred for 7 h and cast onto Al foil. After drying at 90 °C for 12 h, the LFP-based cathode layer was punched into disks (12 mm in diameter), with a mass loading of ~1.8 mg cm^{-2} LFP. High mass loading cathodes, containing either LFP (~10.3 mg cm^{-2}) or NMC811 (~7.7 mg cm^{-2}), were also prepared by mixing active material/Super P/PVDF with a weight ratio of 9:0.5:0.5.

Physical characterizations: FTIR was performed by a Bruker Vertex 70 FTIR spectrometer. Raman technology was performed by an InVia Renishaw Raman spectrometer. NMR was performed by Mercury VX 300 (Varian) to analyze the ^{1}H and ^{13}C spectrum. SEM (JEOL-6390) was used to investigate the surface morphology of LMA and C/S cathodes. XPS was recorded using a PHI5600 X-ray photoelectron spectrometer. The cycled Li metal anodes for recording XPS were washed with DME and stored in the glovebox before testing.

Electrochemical characterizations: All cells/batteries for electrochemical characterizations were assembled within a glovebox (Super 1220/750, Mikrouna). Ionic conductivity (σ) of QSSEs was calculated using

$$\sigma = \frac{L}{RA} \tag{2}$$

where A is the cross-sectional area of the SS (SS = stainless steel) electrodes, L is the distance between two SS electrodes, R is the measured ohmic resistance of a SS|QSSE|SS symmetric cell as obtained from the EIS. EIS was obtained within the frequency range of 7 MHz to 1 Hz using the Bio-Logic VSP-300 electrochemical workstation. The t_{Li}^+ was calculated according to following formula:

$$t_{Li^+} = \frac{I_s(\Delta V - I_0 R_0)}{I_0(\Delta V - I_s R_s)} \tag{3}$$

where the I_0 and I_s are the initial and steady-state currents obtained by the chronoamperometry method, ΔV is the polarization potential of 10.0 mV, and R_0 and R_s are, the initial and steady-state resistances observed from EIS, respectively. To determine the oxidation potential, LSV was conducted on a Li|QSSE|SS cell with a potential range of 1-6 V at a scan rate of 5 mV s^{-1}. Ionic conductivity test and LSV test were measured using the Bio-Logic VSP-300 electrochemical workstation.

Li symmetric cells and batteries were tested using a CT2001A battery testing system (LANHE). Li-S batteries were measured within the voltage range of 1.8-2.5 V. Pouch-type Li-S cells were measured at 0.1 C. Coin-type Li-S batteries were measured at 0.1 C for the first three cycles, and then the charge/discharge rates were changed to 0.3 C for long-term cycling.
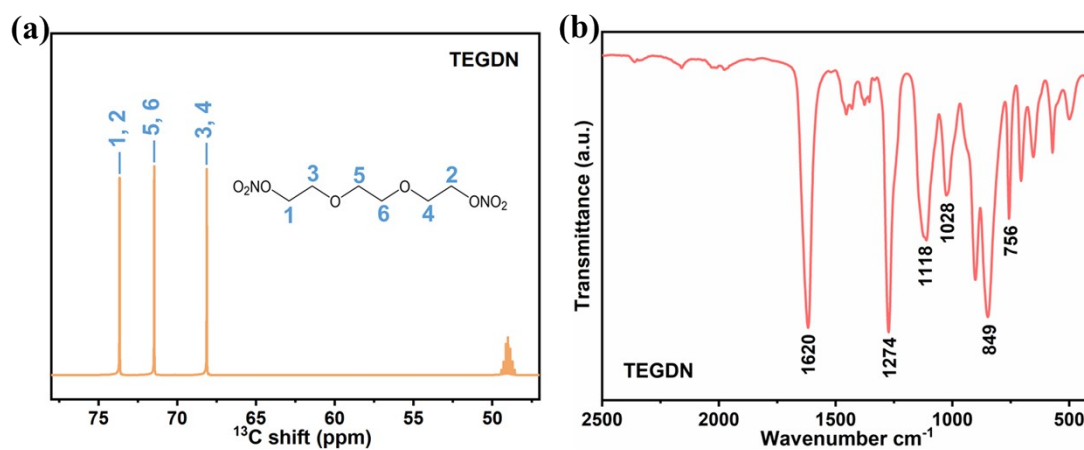
Figures & tables.

Fig. S1 (a) ^{13}C NMR data of TEGDN. (b) FTIR spectrum of TEGDN.

Note:

In TEGDN[15]:

1620 cm^{-1} indicates antisymmetric stretching vibration of -NO$_2$,

1274 cm^{-1} indicates symmetrical stretching vibration of -NO$_2$,

1118 cm^{-1} indicates antisymmetric stretching vibration of C-O-C,

1028 cm^{-1} indicates stretching vibration of N-O,

849 cm^{-1} indicates flexural vibration -NO$_2$,

756 cm^{-1} indicates plane rocking vibration of -CH$_2$.
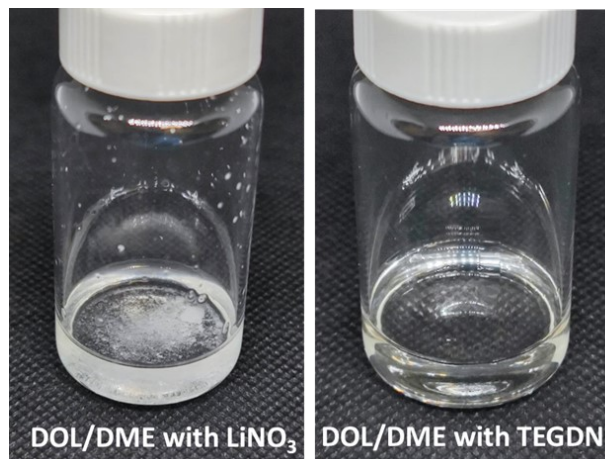
Fig. S2 Digital images of DOL/DME (v:v=1:1) and 0.8 M $LiNO_3$ after 10 days (left), and DOL/DME (v:v=1:1) and 2 M TEGDN after 10 days (right).

Fig. S3 Digital images of DOL/DME (v:v=1:1, with 1 M LiTFSI) after *in situ* polymerization (6 hours).
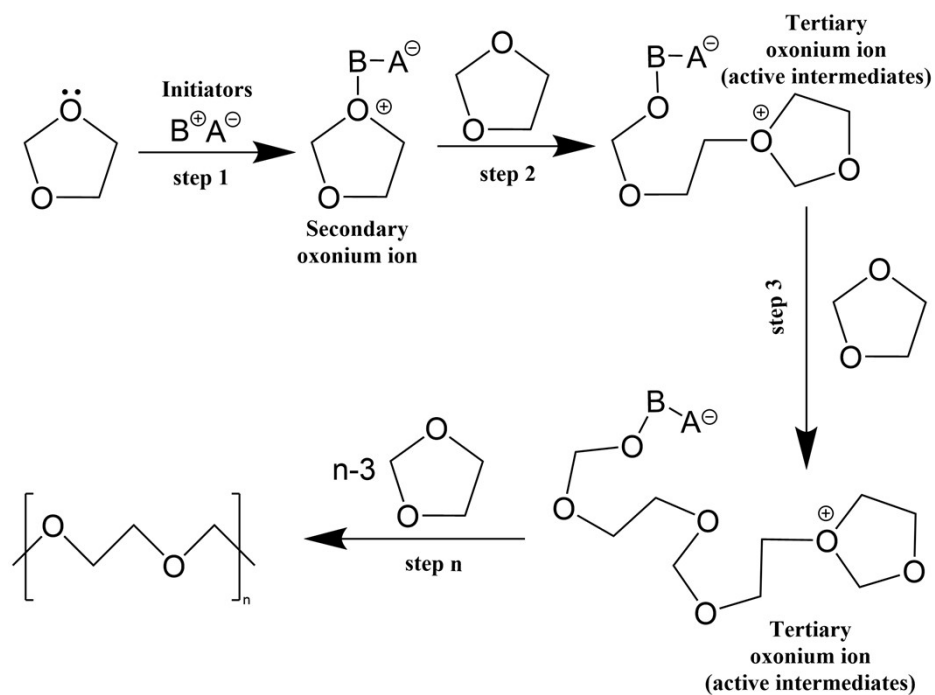
Fig. S4 Basic mechanism of ring-opening polymerization of poly-DOL.

Note: $B^{\oplus}A^{\ominus}$ in this work presents $H^{\oplus}[PF_5OH]^{\ominus}$ generated from the following process:

$$PF_5 + H_2O \rightarrow [PF_5 \cdot H_2O] \rightarrow H^{\oplus}[PF_5OH]^{\ominus}$$

This initiator can be replaced by $Al(OTf)_3$[16], $LiDFOB$[17] and other initiators.
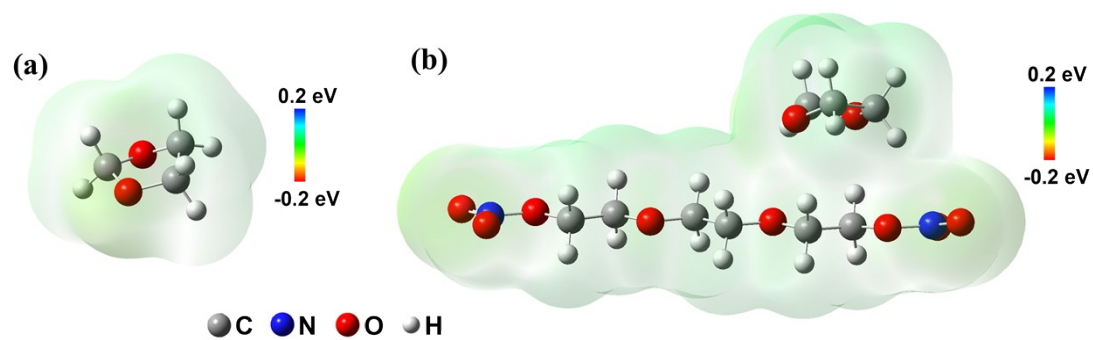
Fig. S5 Electrostatic potential surfaces of (a) pure DOL and (b) DOL with TEGDN.
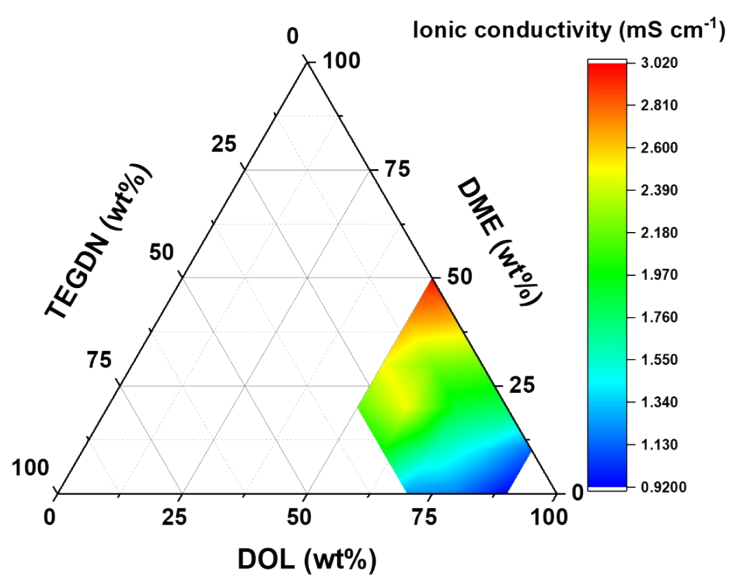
Fig. S6 Ion conductivity of different QSSE compositions. All polymerization times were controlled at ~7 hours.
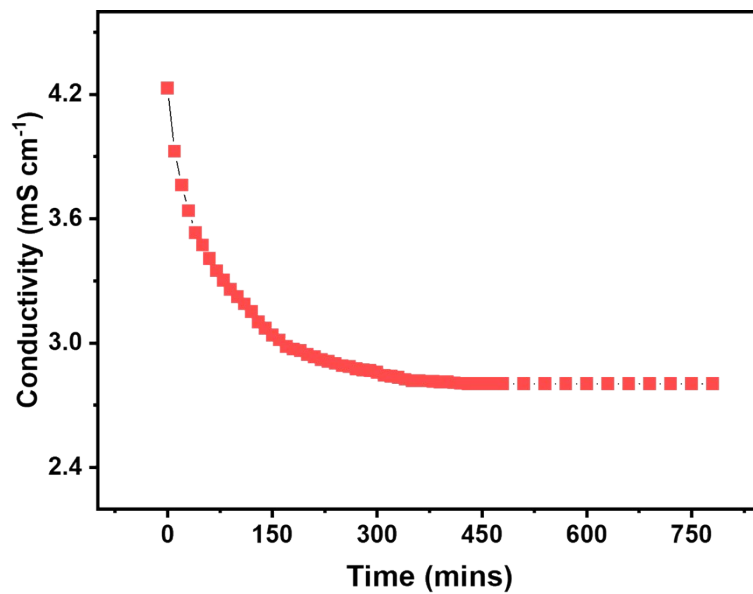
Fig. S7 Li$^+$ of ionic conductivity *vs.* time during *in situ* polymerization of the TEGDN-

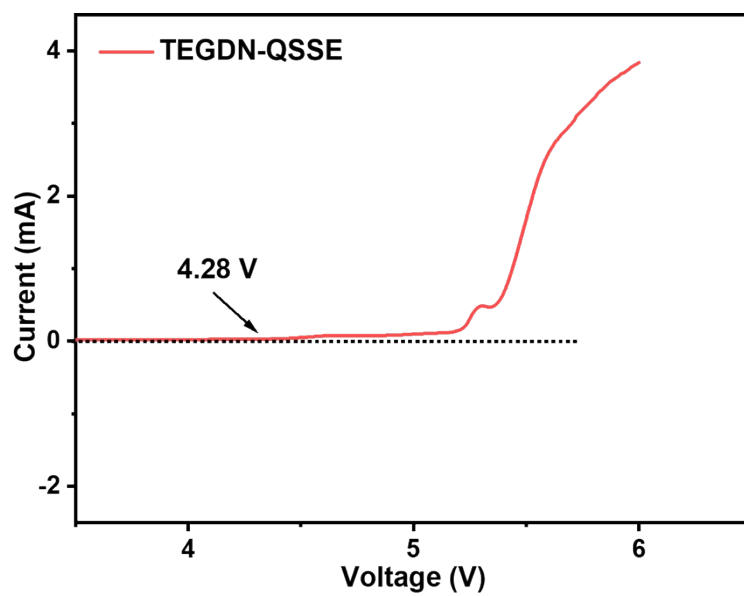QSSE (50 wt% DOL, 45 wt% DME and 5 wt% TEGDN, with 1 M LiTFSI).

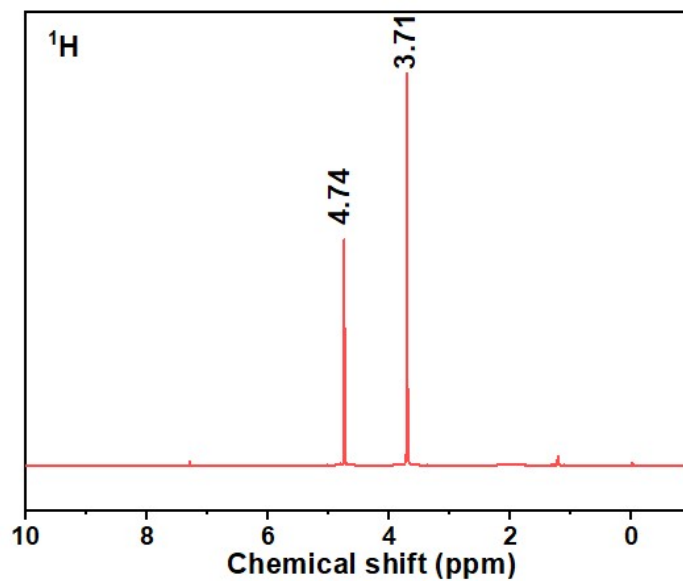Fig. S8 LSV result of TEGDN-QSSE (50 wt% DOL, 45 wt% DME and 5 wt% TEGDN, with 1 M LiTFSI).

Fig. S9 ^{1}H NMR spectrum of the TEGDN-QSSE after ethanol washing.

Note: The chemical shift at 4.75 ppm is assigned to the H on group –O–CH$_2$–O– and 3.72 ppm represents the H on group –O–CH$_2$–CH$_2$–O–[18]. The integral area ratio of these two chemical shift peaks is approximately 1:2, demonstrating that the structure is –CH$_2$–O–CH$_2$–CH$_2$-O–, which matches with the ^{1}H NMR of pure poly-DOL[18].
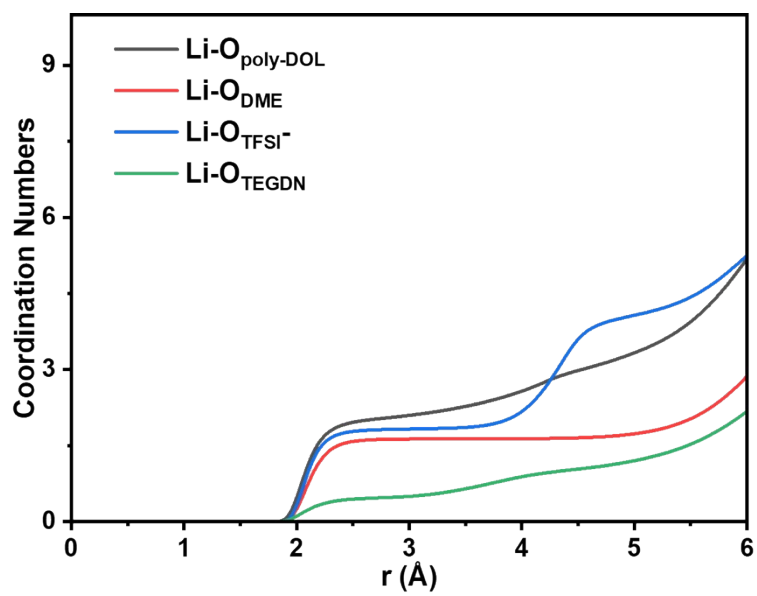
Fig. S10 Coordination number plots of Li–$O_{poly\text{-}DOL}$, Li–O_{DME}, and Li–O_{TFSI}^-, and Li–O_{TEGDN} pairs in TEGDN-QSSE.
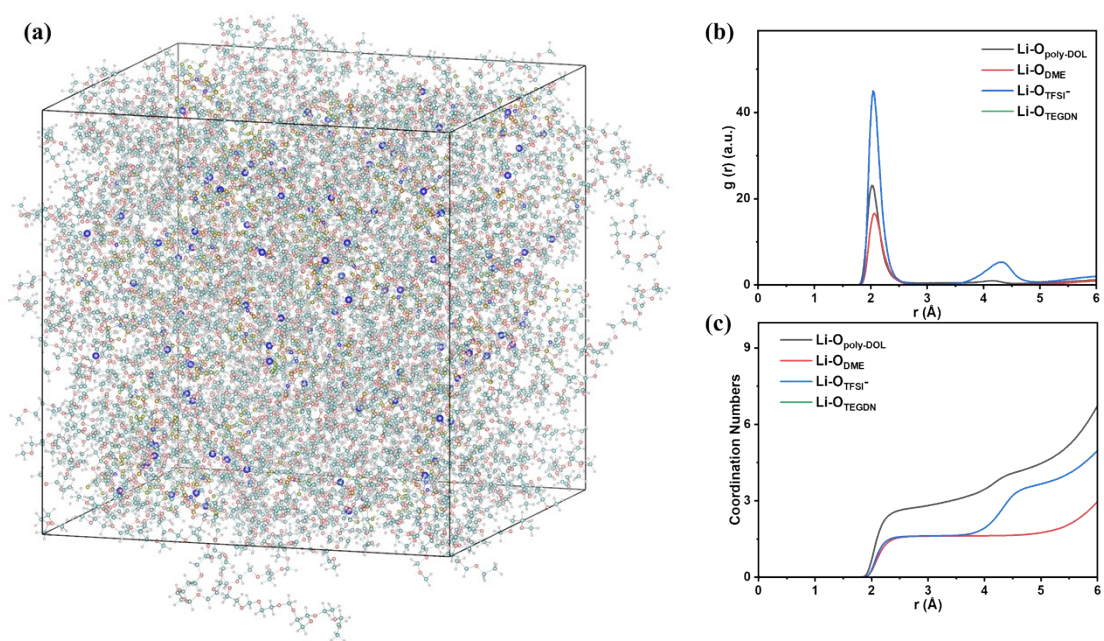
Fig. S11(a) Snapshots of the MD simulation boxes of QSSE without TEGDN. (b) The radial distribution function and (c) coordination number plots of Li–O$_{poly\text{-}DOL}$, Li–O$_{DME}$, and Li–O$_{TFSI}^-$ pairs in QSSE without TEGDN.
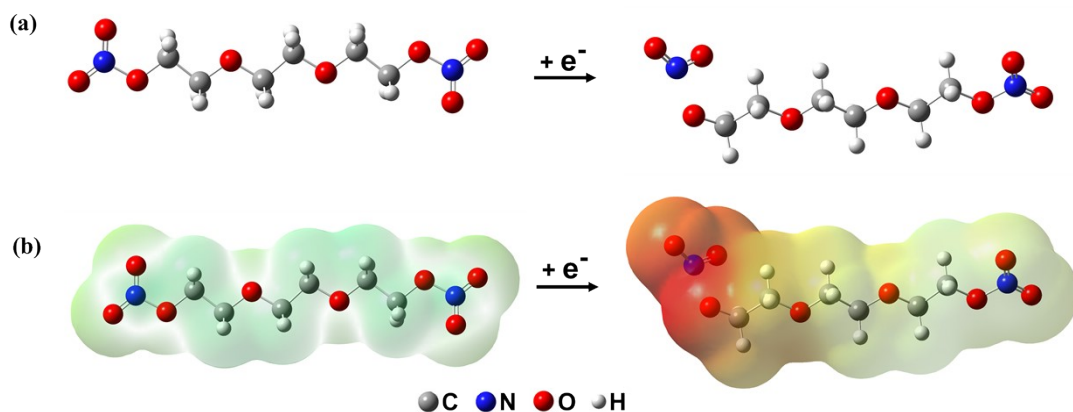
(a)

+ e⁻

(b)

+ e⁻

●C ●N ●O ◐H

Figure S12 (a) The molecular structure and (b) the electrostatic potential surface of TEGDN in the original state (left), and the reductive state (right) after obtaining one single electron.

Note: the structural optimization of TEGDN after obtaining one single electron shows that N-O bond adjacent to the main chain breaks first, and the electrostatic potential result demonstrates that the negative electric field is concentrated in the broken N-O bond.
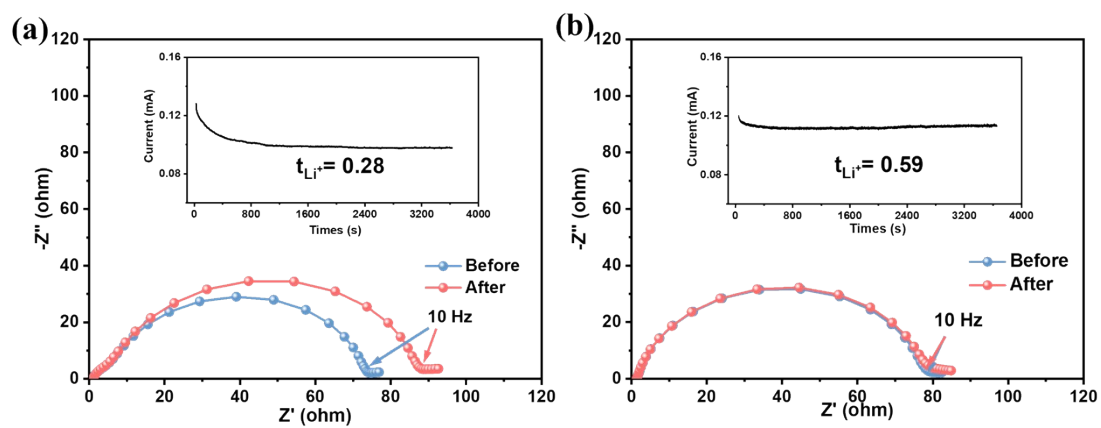
Fig. S13 Nyquist and chronoamperometric plots of (a) Li | liquid electrolyte with TEGDN | Li at 23 °C and (b) Li | QSSE without TEGDN | Li at 23 °C.
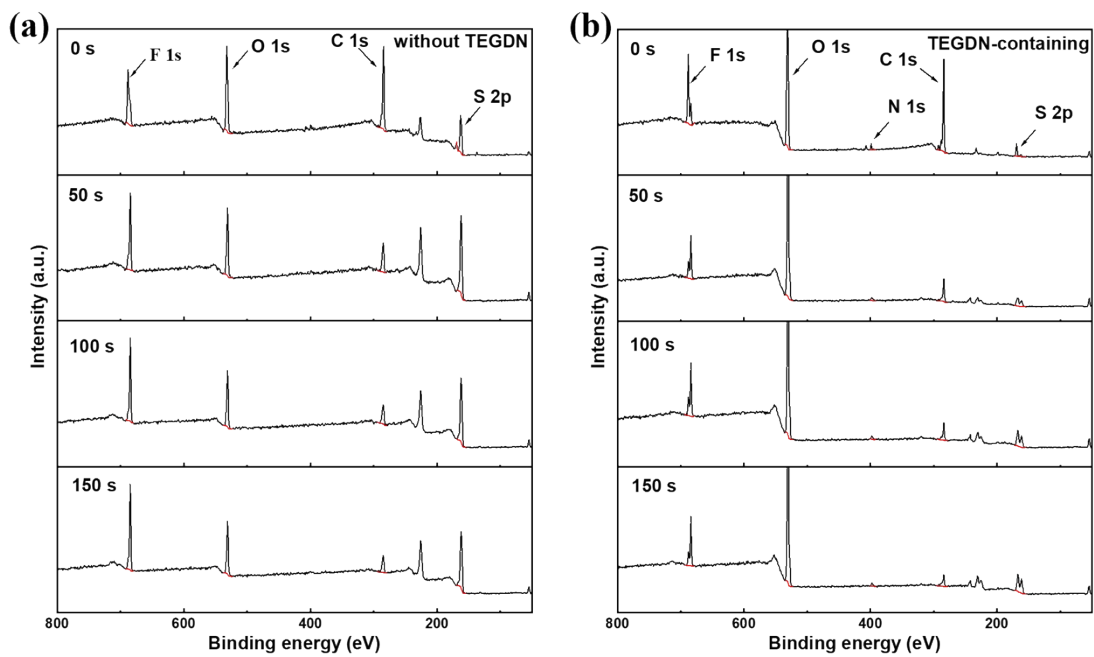
Fig. S14 XPS spectra of LMA (a) without and (b) with TEGDN at various etching times

(0s, 50s, 100s and 150s).

Note: For these experiments, the LMA was taken from QSSE-based Li-S batteries
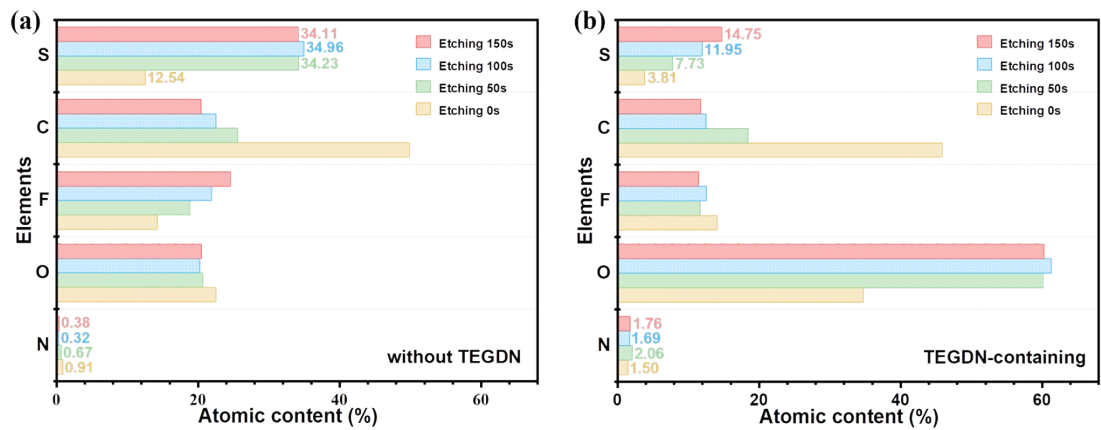
cycled 30 times.

Fig. S15 Atomic content of different elements in the LMA (a) without and (b) with TEGDN at various etching times (0s, 50s, 100s and 150s).

Note: For these experiments, the LMA was taken from QSSE-based Li-S batteries cycled 30 times.
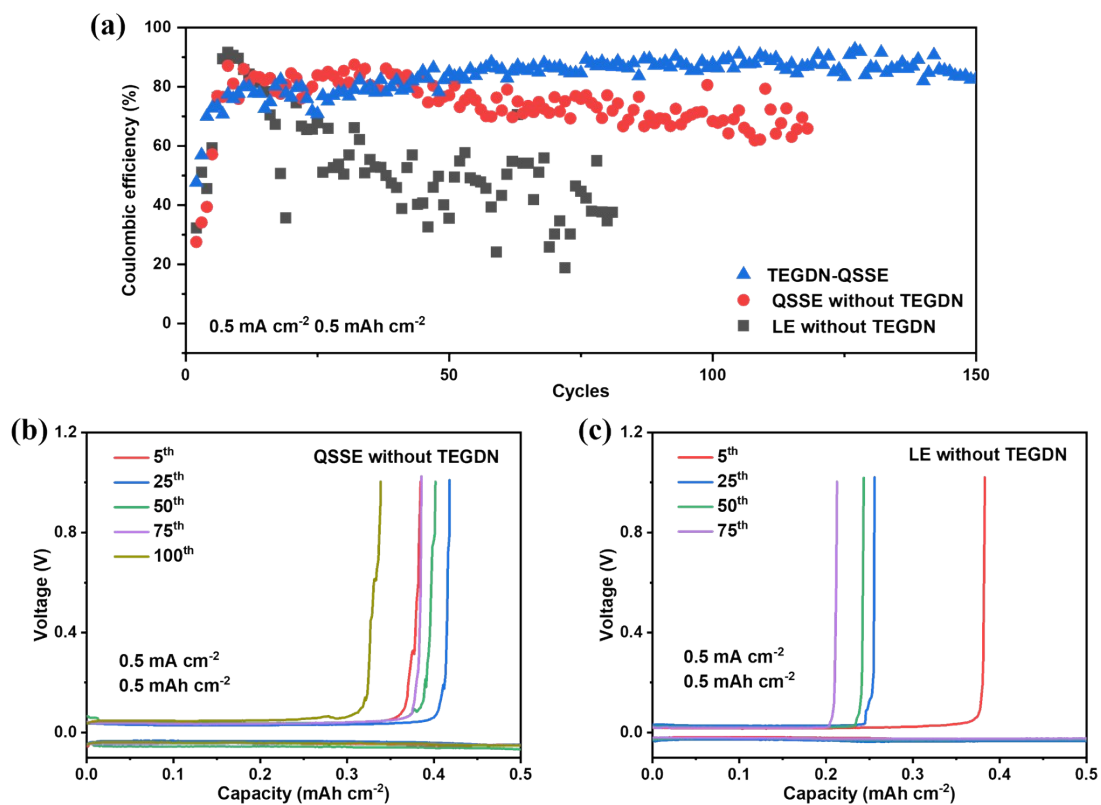
Fig. S16 (a) Cycling performance of Li|Cu cells with the TEGDN-QSSE, the QSSE without TEGDN, and the liquid electrolyte without TEGDN. Typical charge & discharge curves of the Li|Cu cells with (b) the QSSE without TEGDN and (c) the liquid electrolyte without TEGDN.

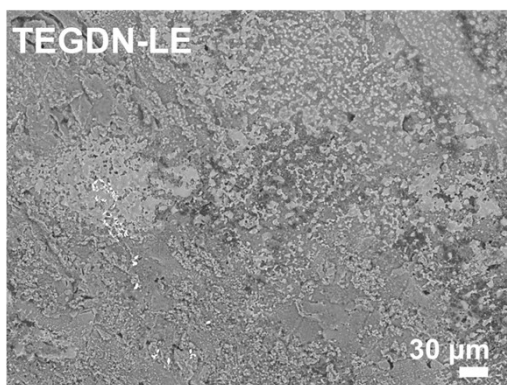Fig. S17 SEM image of liquid electrolyte with TEGDN battery after 30 cycles.

Note: The LMA corresponding to the liquid electrolyte with TEGDN exhibited fewer lithium dendrites and displayed minor pulverization than liquid electrolytes without TEGDN. Yet, the presence of numerous pits still suggests uneven lithium deposition. All the LMAs for SEM images were collected from Li-S batteries cycled 30 times.

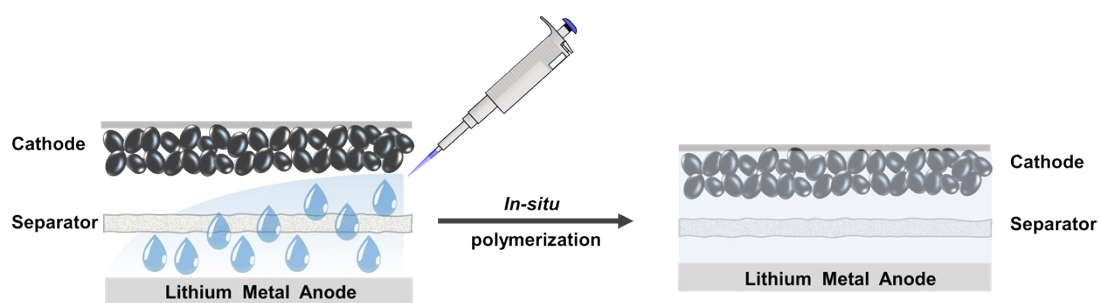Fig. S18 Schematic illustration of integrated coin-type battery production via *in situ* polymerization.
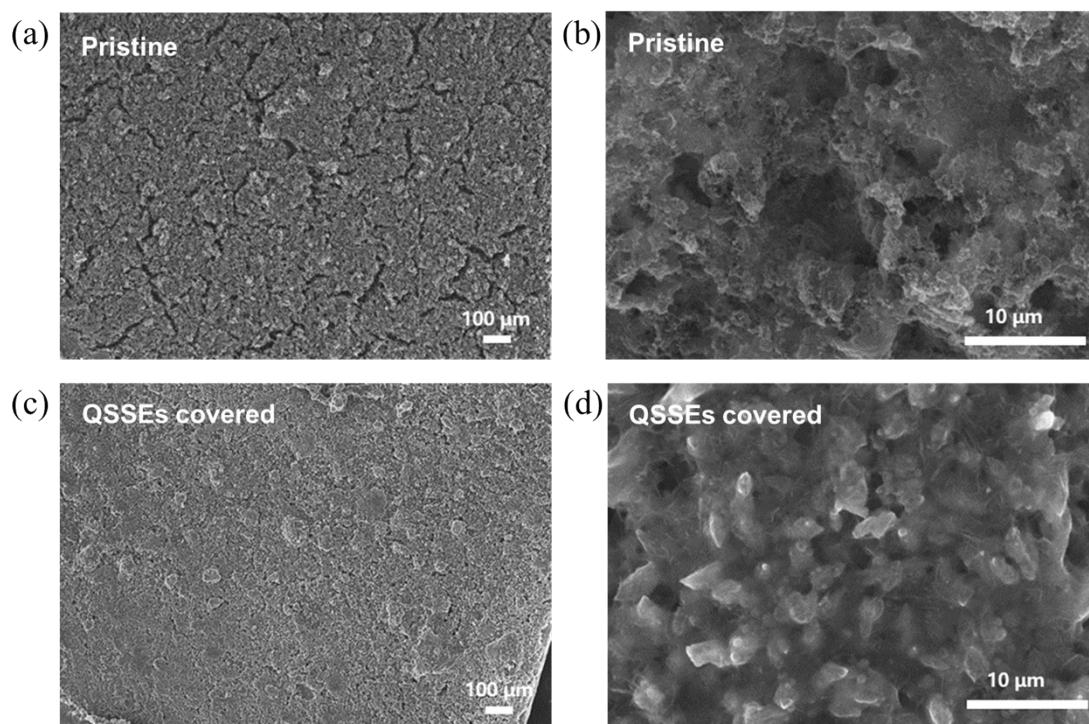
Fig. S19 (a) & (b) SEM images of pristine cathode. (c) & (d) SEM images of cathode after the *in situ* polymerization of the poly-DOL.
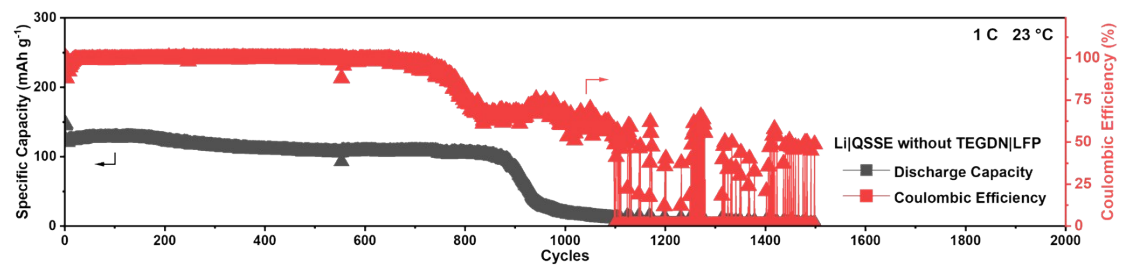
Fig. S20 Cycling performance (1 C) of coin-type battery in the Li|QSSE without TEGDN|LFP configuration.
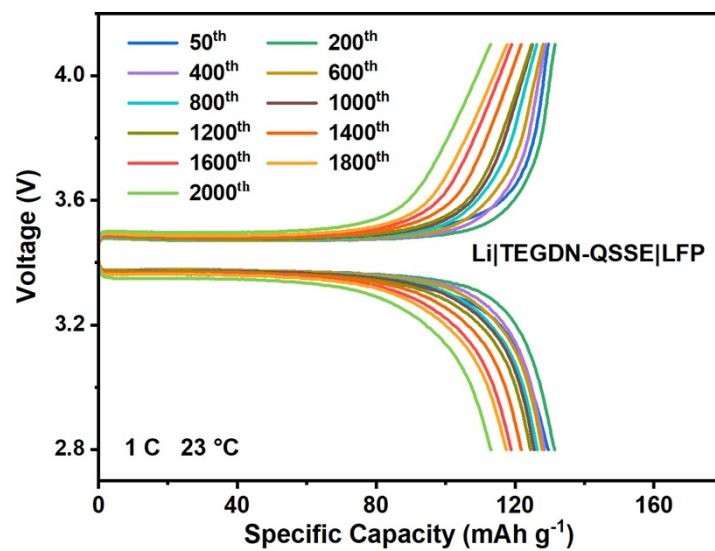
Fig. S21 Charge & discharge curves (1 C) of the Li|TEGDN-QSSE|LFP coin-type battery.
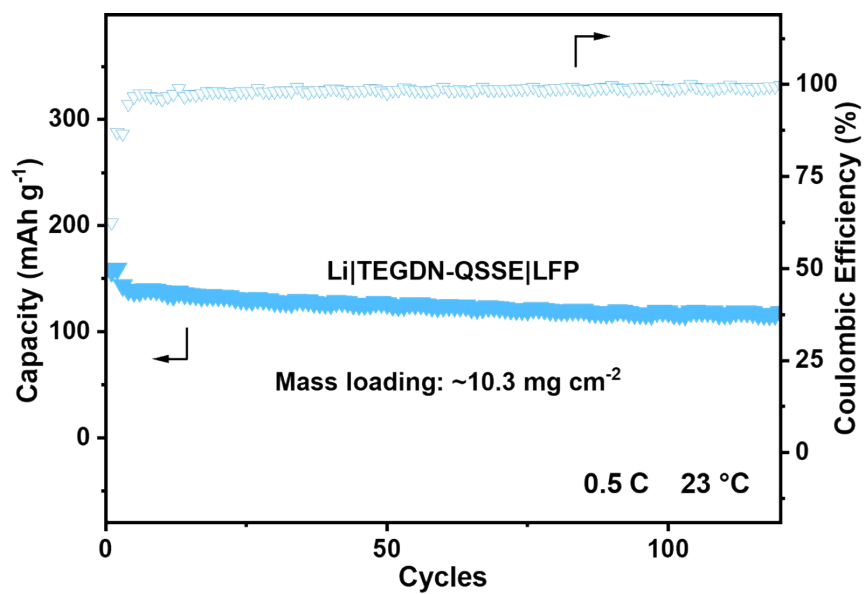
Fig. S22 Cycle performance (0.5 C) of the high loading (~10.3 mg cm^{-2} for LiFePO$_4$) Li|TEGDN-QSSE|LiFePO$_4$ coin-type battery.
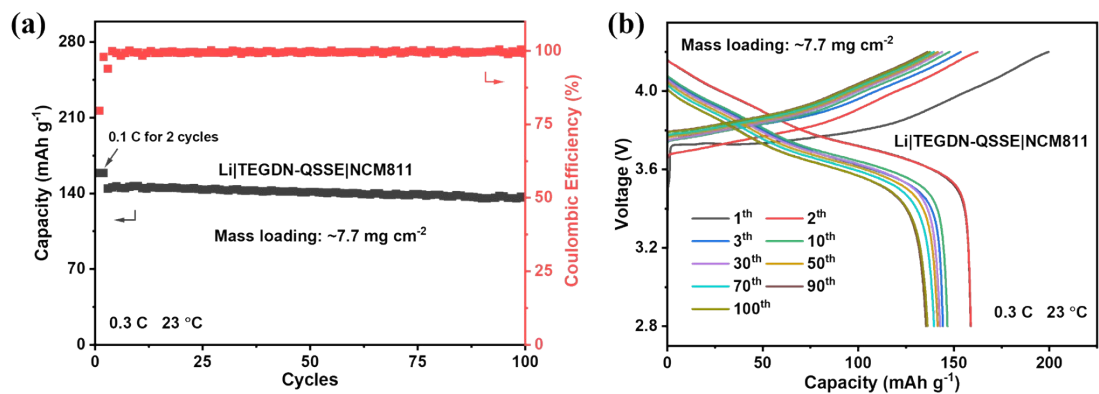
Fig. S23 (a) Cycle performance and (b) Charge & discharge curves of high loading (~7.7mg cm^{-2} for NCM811) Li|TEGDN-QSSE|NCM811 cell. The voltage range was from 2.8 V to 4.2 V. The charge & discharge rates were set at 0.1 C for the first two cycles, and 0.3 C from the 3rd cycle onwards.
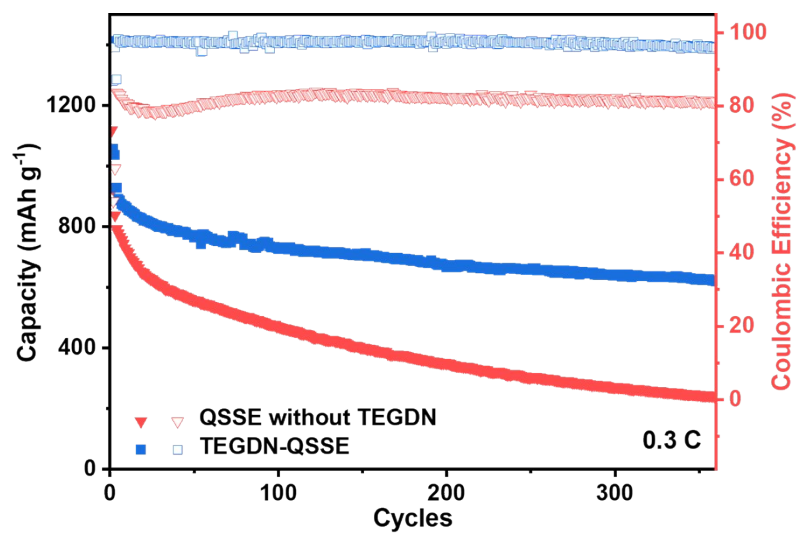
Fig. S24 Coin-type Li-S battery of QSSE without TEGDN and TEGDN-QSSE at 0.3 C.
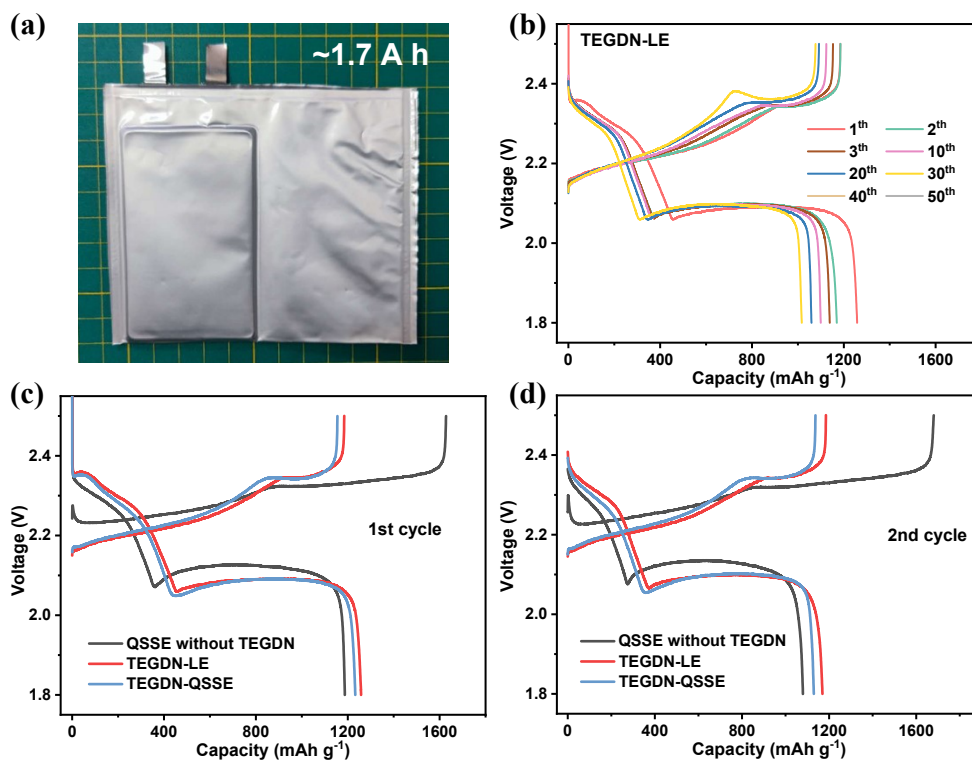
Fig. S25 (a) Digital image of the 1.7 Ah Li-S pouch-type cell used in the cycling test. (b) Charge and discharge curves of TEGDN-containing, pouch-type Li-S battery with a liquid electrolyte (TEGDN-LE). Charge and discharge curves at the (c) first and (d) second cycle for different cells.
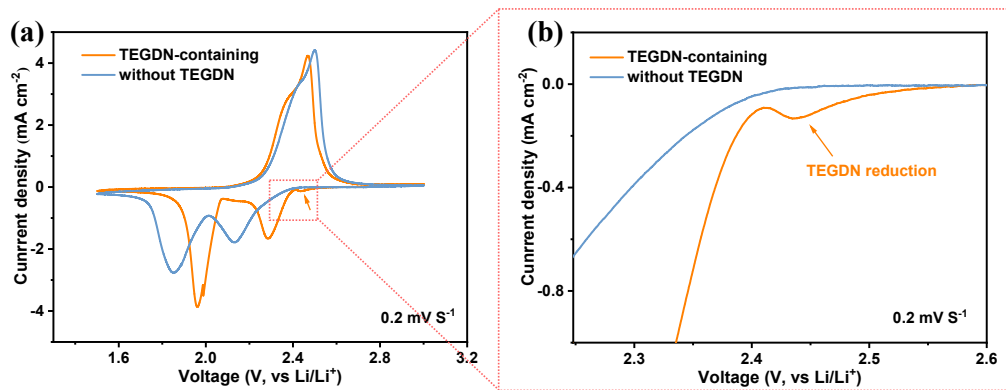
Fig. S26 CV curves of battery without TEGDN and TEGDN-containing QSSE battery.
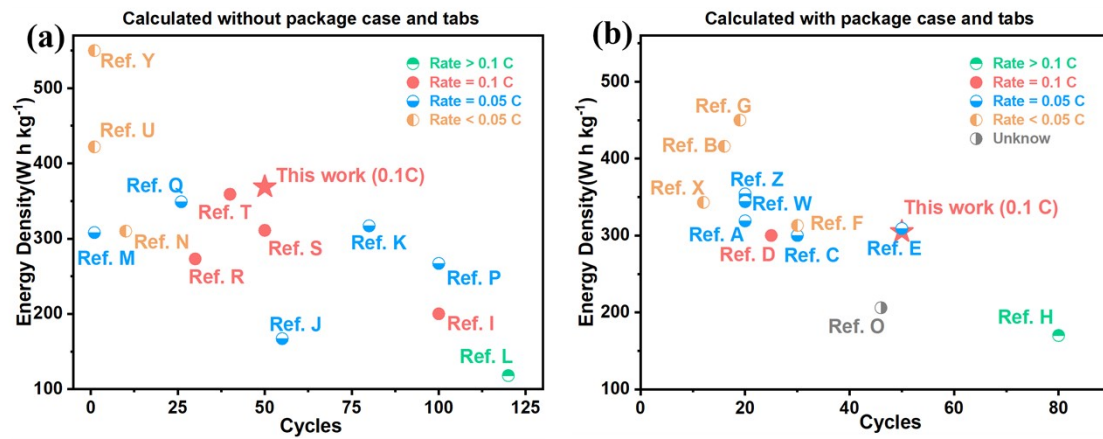
Fig. S27 Summary of performances of state-of-the-art pouch-type Li-S cells, compared with energy density, cycles, and C-rates.

Table S1 | ^{1}H NMR data analysis of TEGDN

Chemical shift/ppm	Corresponding H
3.67	e, f-H
3.82, 3.81, 3.80	c, d-H
4.69, 4.68, 4.67	a. b-H

Table S2 | ^{13}C NMR data analysis of TEGDN

Chemical shift/ppm	Corresponding C
68.13	3, 4-C
71.47	5, 6-C
73.66	1, 2-C

Table S3 | Dissolution properties of $LiNO_3$ and TEGDN in the electrolyte of DOL/DME
(v:v=1:1)

	$LiNO_3$	TEGDN
0.5 M	√	√
0.8 M	×	√
1 M	×	√
2 M	×	√

Note: The tick mark presents completely dissolved and cross mark presents incompletely dissolved.

Table S4 | Partial calculated molecular parameters of original DOL, DOL with $LiNO_3$, and DOL with TEGDN.

	O-C-C-O dihedral angle of	H-C-C mean bond angle
Original DOL	155.55°	112.52°
DOL with $LiNO_3$	172.21°	111.48°
DOL with TEGDN	167.45°	112.51°

Note: The alterations of O-C-C-O dihedral angles and mean H-C-C bond angles of DOL molecules within original DOL, DOL with $LiNO_3$, and DOL with TEGDN demonstrate the DOL molecule structures are significantly changed because of its coordination with $LiNO_3$.

Table S5 | Gel permeation chromatography (GPC) results of QSSE with TEGDN & QSSE without TEGD.

Sample name	Number-average molecular weight (M_n)	Polymerization degree
QSSE without TEGDN	1145	15.47
QSSE with TEGDN	1188	16.05

Note: The samples were washed with ethanol to eliminate residual solvents and lithium salts before measurement. The polymerization degree was calculated by M_n/M_0, where M_0 is the molecular weight of the monomer unit.

Table S6 | Comparison of Li-S pouch cell performance and energy density (calculated

with package and tabs) with recently reported works.

	Energy density (W h kg^{-1})	C-rate	Cycles	Calculated with package and tabs (Y) or not (N)	Year
This work	**304**	**0.1**	**50**	**Y**	**2023**
This work	**368**	**0.1**	**50**	**N**	**2023**
Ref. A[19]	319	0.05	20	Y	2022
Ref. B[20]	416	0.05	16	Y	2022
Ref. C[21]	300	0.05	30	Y	2021
Ref. D[22]	300	0.1	25	Y	2021
Ref. E[23]	309	0.05	50	Y	2022
Ref. F[24]	313	0.02	30	Y	2021
Ref. G[25]	450	0.015	19	Y	2022
Ref. H[26]	80	0.2	170	Y	2020
Ref. I[27]	200	0.1	100	N	2021
Ref. J[28]	167	0.05	55	N	2021
Ref. K[29]	317	0.05	80	N	2021
Ref. L[30]	118	0.14	120	N	2021
Ref. M[31]	308	0.05	1	N	2021
Ref. N[32]	310	0.02	10	N	2022
Ref. O[33]	206	unknown	46	Y	2021
Ref. P[34]	267	0.05	100	N	2021
Ref. Q[35]	349	0.06	26	N	2021
Ref. R[36]	273	0.1	30	N	2022
Ref. S[37]	311	0.07	50	N	2022
Ref. T[38]	259	0.1	40	N	2022
Ref. U[39]	422	0.025	1	N	2022
Ref. V[40]	350	0.05	25	Y	2022
Ref. W[41]	344	0.05	20	Y	2022
Ref. X[42]	343	0.025	12	Y	2021
Ref. Y[43]	550	0.005	1	N	2022
Ref. Z[43]	354	0.05	20	Y	2022

References

1. M. J. Abraham, T. Murtola, R. Schulz, S. Páll, J. C. Smith, B. Hess and E. Lindahl, SoftwareX, 2015, 1-2, 19-25.

2. W. L. Jorgensen, D. S. Maxwell and J. Tirado-Rives, Journal of the American Chemical Society, 1996, 118, 11225-11236.

3. T. Lu and F. Chen, Journal of Computational Chemistry, 2012, 33, 580-592.

4. T. Lu and F.-W. Chen, Acta Physico-Chimica Sinica, 2012, 28, 1-18.

5. B. Hess, Journal of Chemical Theory and Computation, 2008, 4, 116-122.

6. L. Martínez, R. Andrade, E. G. Birgin and J. M. Martínez, Journal of Computational Chemistry, 2009, 30, 2157-2164.

7. U. Essmann, L. Perera, M. L. Berkowitz, T. Darden, H. Lee and L. G. Pedersen, The Journal of Chemical Physics, 1995, 103, 8577-8593.

8. T. Darden, D. York and L. Pedersen, The Journal of Chemical Physics, 1993, 98, 10089-10092.

9. K. Momma and F. Izumi, Journal of Applied Crystallography, 2011, 44, 1272-1276.

10. M. J. Frisch, G. W. Trucks and et al., Gaussian 09, Revision D.01, Gaussian, Inc., Wallingford CT, 2016, 2016.

11. P. J. Stephens, F. J. Devlin, C. F. Chabalowski and M. J. Frisch, The Journal of Physical Chemistry, 1994, 98, 11623-11627.

12. R. Dennington, T. Keith and J. Millam, GaussView, version 5,, 2009.

13. W. Humphrey, A. Dalke and K. Schulten, Journal of Molecular Graphics, 1996, 14, 33-38.

14. F. Zeng, A. Wang, W. Wang, Z. Jin and Y.-S. Yang, Journal of Materials Chemistry A, 2017, 5, 12879-12888.

15. R. J. Buszek, D. Soto, J. M. Dailey, S. Bolden, T. L. Tall, L. M. Hudgens, C. A. Marshall, J. A. Boatz and G. W. Drake, Propellants, Explosives, Pyrotechnics, 2018, 43, 115-121.

16. Q. Zhao, X. Liu, S. Stalin, K. Khan and L. A. Archer, Nature Energy, 2019, 4, 365-373.

17. Y. Liu and Y. Xu, Chemical Engineering Journal, 2022, 433, 134471.

18. R. Ali, A. Farah and Z. Binkhathlan, Saudi Pharmaceutical Journal, 2017, 25, 258-265.

19. L.-P. Hou, N. Yao, J. Xie, P. Shi, S.-Y. Sun, C.-B. Jin, C.-M. Chen, Q.-B. Liu, B.-Q. Li, X.-Q. Zhang and Q. Zhang, Angewandte Chemie International Edition, 2022, 61, e202201406.

20. X.-Y. Li, S. Feng, C.-X. Zhao, Q. Cheng, Z.-X. Chen, S.-Y. Sun, X. Chen, X.-Q. Zhang, B.-Q. Li, J.-Q. Huang and Q. Zhang, Journal of the American Chemical Society, 2022, 144, 14638-14646.

21. M. Zhao, X. Chen, X.-Y. Li, B.-Q. Li and J.-Q. Huang, Advanced Materials, 2021, 33, 2007298.

22. X.-Q. Zhang, Q. Jin, Y.-L. Nan, L.-P. Hou, B.-Q. Li, X. Chen, Z.-H. Jin, X.-T. Zhang, J.-Q. Huang and Q. Zhang, Angewandte Chemie International Edition, 2021, 60, 15503-15509.

23. W.-G. Lim, C.-Y. Park, H. Jung, S. Kim, S. H. Kang, Y.-G. Lee, Y. C. Jeong, S. B. Yang, K. Sohn, J. W. Han and J. Lee, Advanced Materials, 2022, n/a, 2208999.

24. X. Wang, Y. Yang, C. Lai, R. Li, H. Xu, D. H. S. Tan, K. Zhang, W. Yu, O. Fjeldberg, M. Lin, W. Tang, Y. S. Meng and K. P. Loh, Angewandte Chemie International Edition, 2021, 60, 11359-11369.

25. Z.-X. Chen, L.-P. Hou, C.-X. Bi, Q. Cheng, X.-Q. Zhang, B.-Q. Li and J.-Q. Huang, Energy Storage Materials, 2022, 53, 315-321.

26. J.-Y. Hwang, H. M. Kim and Y.-K. Sun, Journal of The Electrochemical Society, 2018, 165, A5006.

27. G. Xia, Z. Zheng, J. Ye, X. Li, M. J. Biggs and C. Hu, Chemical Engineering Journal, 2021, 406, 126823.

28. J. He, A. Bhargav and A. Manthiram, Advanced Materials, 2020, 32, 2004741.

29. C. Zhao, G.-L. Xu, Z. Yu, L. Zhang, I. Hwang, Y.-X. Mo, Y. Ren, L. Cheng, C.-J. Sun, Y. Ren, X. Zuo, J.-T. Li, S.-G. Sun, K. Amine and T. Zhao, Nature Nanotechnology, 2021, 16, 166-173.

30. L. Luo, J. Li, H. Yaghoobnejad Asl and A. Manthiram, ACS Energy Letters, 2020, 5, 1177-1185.

31. Y. Li, W. Wang, B. Zhang, L. Fu, M. Wan, G. Li, Z. Cai, S. Tu, X. Duan, Z. W. Seh, J. Jiang and Y. Sun, Nano Letters, 2021, 21, 6656-6663.

32. Y. Li, T. Gao, D. Ni, Y. Zhou, M. Yousaf, Z. Guo, J. Zhou, P. Zhou, Q. Wang and S. Guo, Advanced Materials, 2022, 34, 2107638.

33. Y. Huang, M. Shaibani, T. D. Gamot, M. Wang, P. Jovanović, M. C. Dilusha Cooray, M. S. Mirshekarloo, R. J. Mulder, N. V. Medhekar, M. R. Hill and M. Majumder, Nature Communications, 2021, 12, 5375.

34. T. Liu, Z. Shi, H. Li, W. Xue, S. Liu, J. Yue, M. Mao, Y.-s. Hu, H. Li, X. Huang, L. Chen and L. Suo, Advanced Materials, 2021, 33, 2102034.

35. J. Lian, W. Guo and Y. Fu, Journal of the American Chemical Society, 2021, 143, 11063-11071.

36. J. He, A. Bhargav and A. Manthiram, Advanced Energy Materials, 2022, 12, 2103204.

37. Z. Han, S. Li, R. Xiong, Z. Jiang, M. Sun, W. Hu, L. Peng, R. He, H. Zhou, C. Yu, S. Cheng and J. Xie, Advanced Functional Materials, 2022, 32, 2108669.

38. S. Li, J. Lin, B. Chang, D. Yang, D.-Y. Wu, J. Wang, W. Zhou, H. Liu, S. Sun and L. Zhang, Energy Storage Materials, 2023, 55, 94-104.

39. G. Ye, M. Zhao, L.-P. Hou, W.-J. Chen, X.-Q. Zhang, B.-Q. Li and J.-Q. Huang, Journal of Energy Chemistry, 2022, 66, 24-29.

40. L.-P. Hou, X.-Y. Li, C.-X. Bi, Z.-X. Chen, Z. Li, L.-L. Su, P. Shi, C.-B. Jin, B.-Q. Li, J.-Q. Huang, X.-Q. Zhang and Q. Zhang, Journal of Power Sources, 2022, 550, 232144.

41. Y.-Q. Peng, M. Zhao, Z.-X. Chen, Q. Cheng, Y. Liu, X.-Y. Li, Y.-W. Song, B.-Q. Li and J.-Q. Huang, Nano Research, 2022, DOI: 10.1007/s12274-022-4584-z.

42. C.-X. Zhao, X.-Y. Li, M. Zhao, Z.-X. Chen, Y.-W. Song, W.-J. Chen, J.-N. Liu, B. Wang, X.-Q. Zhang, C.-M. Chen, B.-Q. Li, J.-Q. Huang and Q. Zhang, Journal of the American Chemical Society, 2021, 143, 19865-19872.

43. Y.-Q. Peng, M. Zhao, Z.-X. Chen, Q. Cheng, Y. Liu, C.-X. Zhao, X. Ma, B.-Q. Li, C.-M. Chen, J.-Q. Huang and Q. Zhang, Batteries & Supercaps, 2022, 5, e202100359.